Modal parameter tuning of an axisymmetric resonator via mass perturbation

David Schwartz, Dennis Kim, Phil Stupar, Jeff DeNatale, and Robert T. M'Closkey, *Member, IEEE*

***Abstract*—This paper reports the permanent frequency mismatch reduction of the primary wine glass modes in a planar axisymmetric resonator by strategic mass loading. The resonator consists of a set of concentric rings that are affixed to neighboring rings by a staggered system of spokes. The outer layers of spokes are targets for mass deposition. The paper develops modified ring equations that guide the mass perturbation process and despite the fact that the eposited mass and deposition locations are quantized, it is possible to systematically reduce the frequency difference of the wine glass modes to effective degeneracy such that two modes cannot be distinguished in a frequency response plot. Results on five resonators are reported with nominal wine glass modes near 14 kHz, quality factors of 50 k, and frequency mismatches exceeding 30 Hz in some cases but with post-perturbation mismatches smaller than 80 mHz. Furthermore, it is also shown that the quality factors remain unchanged.**

***Index Terms*—Gyroscopes, microsensors, sensor phenomena and characterization**

I. Introduction

This paper develops an integrated testing and modeling approach to support the systematic and permanent modification of the dynamics of a micromachined axisymmetric resonator and culminates in the demonstration of modal frequency matching of the first pair of "wine glass" modes. Instead of ablation or electrostatic tuning, the resonator was designed to accommodate two types of mass loading at specific locations on the resonator. The interest in matching the modal frequencies derives from the increase in the signal-to-noise ratio of the angular rate estimate when the resonator is used as a closed-loop coriolis vibratory gyro (CVG) under the condition that the electrical noise associated with the pick-off signal conditioning circuits is the dominant noise source [1]. Matched modal frequencies also facilitate the operation of the resonator as a whole angle gyroscope [2]. The resonator introduced in this paper is a bulk micromachined planar structure that is axisymmetric under discrete rotations so, consequently, the theory most relevant to this resonator are the results developed for modifying the dynamics of rings. For example, [3], [4], [5] address thin rings where it is assumed that the deviation from perfect symmetry is small, so consequently the required perturbations to the ring mass and stiffness to bring pairs of modes to degeneracy are small compared to their nominal values.

This work was supported by DARPA contract W31P4Q-11-1-0004.

D. Schwartz, D. Kim, and R.T. M'Closkey are with the Mechanical and Aerospace Engineering Department, University of California, Los Angeles.

P. Stupar and J. DeNatale are with Teledyne Scientific & Imaging, LLC.

R.T. M'Closkey is corresponding author; 38-137 Engineering 4, UCLA, Los Angeles, CA, 90095-1597; ph. 310 825-2909.

Microscale resonators present special challenges, though, because even with a sound theory to guide the perturbation process, the physical means to create the perturbation will often be constrained by the resonator size and compatibility with its fabrication technique. The literature for MEM CVGs is quite extensive so this brief review is limited to microscale axisymmetric resonators and excludes designs such as tuning forks. The most ubiquitous approach to modifying the dynamics of microscale resonators is to employ electrostatic force gradients to modify the effective stiffness associated with one or more modes. For planar axisymmetric resonators this approach has been successfully used for some time [6], [7], and is still employed because of its simple and effective implementation [8], [9]. More recently, a number of fabrication results have been published on microscale three-dimensional resonators. The effects of electrostatic biasing or outright modal frequency tuning has been reported for hemispheres [10], [11], hemitoroids [12], [13], and cylinders [14]. Few results, however, have been reported on the permanent modification of microscale resonators. This is understandable since the fabrication of the resonator itself, much less the development of post-fabrication perturbation techniques, often requires a great deal of innovation.

Permanent modification of the resonator dynamics still holds appeal if only to eliminate the biasing electronics that must produce stable biasing potentials over the sensor operating environment, especially with regard to temperature. There is also the underlying concern that if a mistake is made, it cannot simply be reversed as in the case of electrostatic tuning. Laser ablation has been reported in [15] for reducing the frequency mismatch of a ring resonator, but it appears to be at the expense of the quality factors. Recently, [16] demonstrated a large reduction in frequency mismatch by ablating mass from the rim of a hemispherical resonator. The quality factors were not adversely effected and although the mismatch was reduced by two orders of magnitude, further reduction would still be necessary to take full advantage of the mechanical gain afforded by its high quality factors. Mass deposition, as compared to mass removal, is appealing because potential damage to, or contamination of, the resonator can be avoided and until now no results have been reported in which mass deposition has been used to modify microscale axisymmetric resonators. This paper presents a systematic approach for vastly reducing the detuning frequency of the $n = 2$ pair of modes by strategic mass loading. The resonator introduced in Sec. II accepts the deposition of 75 μm diameter precision solder spheres for coarse point mass perturbations and individual droplets of silver particle-loaded ink for fine

point mass perturbations. These perturbation masses are consistent enough so that the effect on the dynamics of the structure are readily predictable from modified ring models developed in this paper, so despite the fact that the mass is deposited in quantized amounts, the novel resonator design has enough freedom in the deposition locations to render the $n = 2$ wine glass modes effectively degenerate. In other words, the difference in the modal frequencies is less than the mechanical bandwidth of the modes so two distinct peaks cannot be discerned on a frequency response plot. The allowable degree of detuning is dependent on the quality factors and it is shown that the resonator quality factors at the conclusion of the mass deposition remain at their initial values, typically near $50\,\mathrm{k}$ for the $n = 2$ modes that are approximately $14\,\mathrm{kHz}$.

The paper is organized as follows. Sec. II discusses the design and fabrication of the resonator, the mass perturbations and the resonator testing. Sec. III reviews a published model for a ring resonator and under an appropriate assumption, further manipulates it into an intuitive form that relates the pre- and post-perturbation frequency detuning values and anti-node orientations as a function of the point mass perturbations and their location on the resonator. The quantization of the deposited mass leads to the notion of sensitivity parameters and it is described how to empirically estimate these quantities. This section also discusses the parametric modeling of the resonator from multi-channel frequency data. Although the parametric modeling is only superficially discussed because details have been reported elsewhere, it is an integral piece of the tuning algorithm since the modal frequencies and anti-node parameters for a given resonator are derived from analysis of the model. Sec. IV follows a resonator with an initial $n = 2$ detuning frequency of over $25\,\mathrm{Hz}$ through a sequence of three mass depositions that ultimately reduce the detuning to about $60\,\mathrm{mHz}$. Deposition experiments with another four resonators are discussed in Sec. V, and Sec. VI concludes the paper.

II. Resonator Design and Fabrication

The resonator used for the mass deposition and frequency mismatch reduction study is depicted in Fig. 1. The resonator consists of nine concentric rings, each $20\,\mu\mathrm{m}$ in width, which are connected to their neighbors by a staggered system of spokes. The diameter of the outermost ring is $10\,\mathrm{mm}$. The outer ring is surrounded by twenty four discrete electrodes, each of which subtends a 15° arc. Any electrode can be configured for in-plane electrostatic actuation or capacitance sensing. The gap between the electrodes and outer ring sidewall is $20\,\mu\mathrm{m}$. The four outermost layers of spokes are larger and are designed to accommodate mass loading of the structure at these points. Furthermore, in the four outer layers, the spokes are spaced 15° from their neighbors so there are 24 spokes per layer. The outermost layer of spokes have shallow reservoirs etched into them, whereas the remaining large spokes have a $130\,\mu\mathrm{m}$ diameter gold film pad, $1\,\mu\mathrm{m}$ thick, deposited on the top surface. In all, there are 24 reservoirs and 72 gold pads. The reservoirs and pads are visible in Fig. 2.

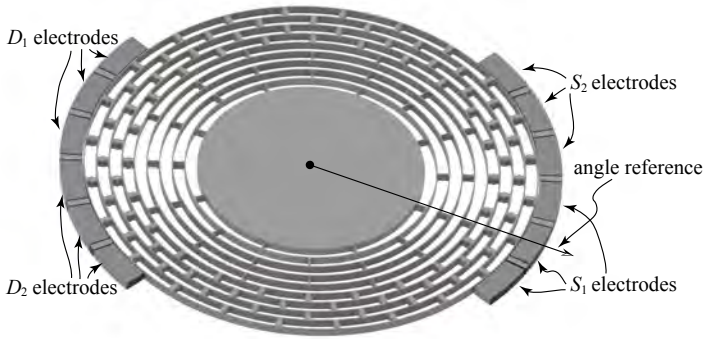

Fig. 1. Isometric view of the resonator with 96 large spokes arranged at four different radii. Mass deposited on the large spokes approximates a point-mass perturbation of the resonator. There are 24 circumferential electrodes, however, only those used for actuation (D_1 and D_2 electrodes) and those used for sensing (S_1 and S_2 electrodes) are shown. The centroid of the S_1 electrode provides a physical reference on the resonator and all angles are measured counterclockwise with respect to this reference.

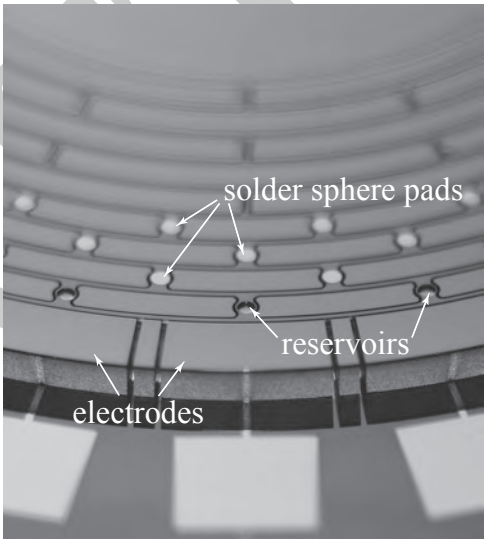

Fig. 2. Detail of resonator showing circumferential electrodes, and reservoirs and gold pads on the large spokes. The central "stem" of the resonator that is bonded to the base wafer is a visible at the top of the photograph.

A. Resonator Fabrication

The resonator is fabricated using a bonded wafer approach. The resonator wafer is 270um thick (111) Si. The base wafer is 450um thick (100) Si. A schematic of the process sequence is shown in Fig. 3. The base wafer is etched to create recessed gaps for clearance of the resonator rings and thermally oxidized for electrical isolation. Openings in the oxide for substrate electrical contact are etched in the oxide layer, and Au metal deposited for the wafer-wafer bonding and electrical connection to the base wafer. Separately, the resonator wafer is patterned with the mating bond metal pattern. The resonator and base wafers are bonded using an aligned Au/Au thermocompression bond process. The Au pads for solder deposition were patterned on the resonator wafer surface of the bonded structure using a deposition and liftoff process. Definition of the resonator rings and reservoir structures is then done using a two-level mask and DRIE etching, see Fig. 4. This uses an oxide layer on the Si opened at

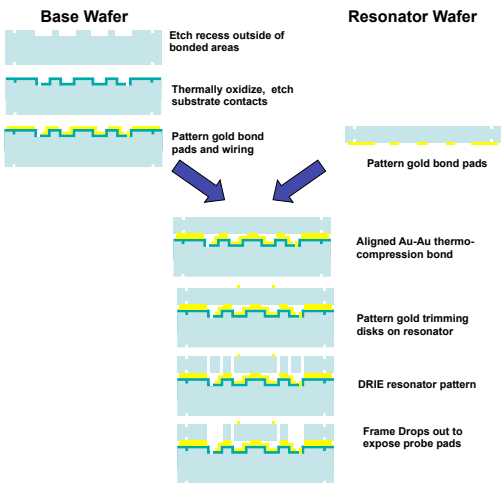

Fig. 3. Process flow for resonator fabrication.

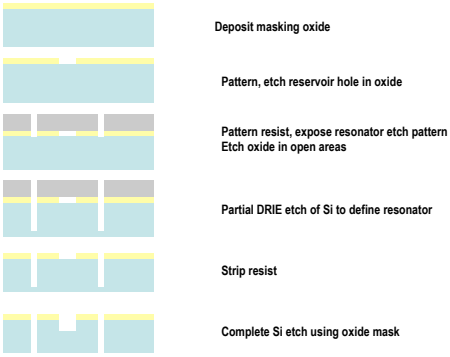

Fig. 4. Reservoir etch and final ring release.

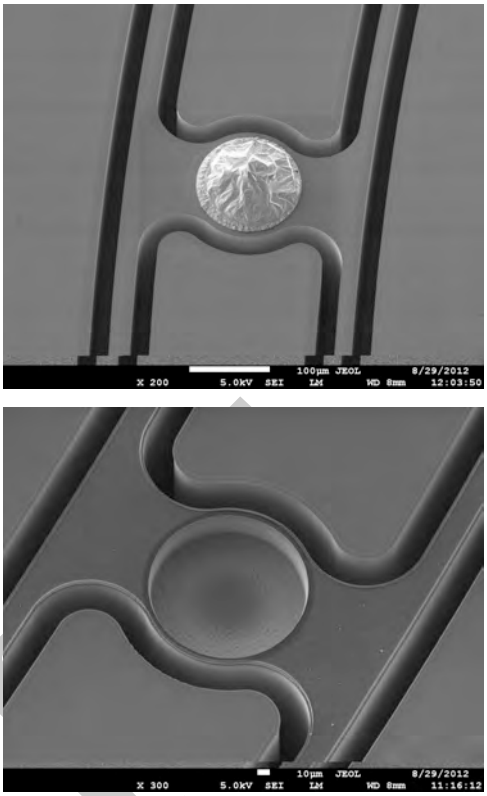

Fig. 5. Top: Reflowed solder sphere on gold pad. Bottom: Silver particle ink deposited into reservoir.

the reservoir locations. A resist mask is subsequently applied and patterned to define the resonator structure. The oxide layer is etched in these locations, and a partial Si DRIE is performed using the same resist mask. The resist is then stripped, and the DRIE etch continued using the oxide mask to complete the etch of the resonator rings through the top wafer thickness, while simultaneously etching the shallow reservoirs into the Si.

B. Mass Perturbations

Two types of mass perturbations are used to modify the resonator dynamics. Coarse perturbations are achieved by depositing and reflowing 75 μm diameter SnAgCu solder spheres (Profound Material Technology) onto the gold pads. Fine perturbations are achieved by depositing individual droplets of silver nano-particle-loaded ink (Cima NanoTech silver conductive ink) into the etched reservoirs. Placement of the solder spheres is achieved with a wire bonder ceramic capillary while individual 60 μm diameter droplets of ink are dispensed using a MicroFab Technologies printhead. Photos of a reflowed solder sphere and a reservoir with ink are shown in Fig. 5.

C. Resonator Testing

The dynamic properties of the $n = 2$ "wineglass" modes are of particular interest so the forcer and pick-off electrodes are customized to excite and measure the response of these modes. The each sensing pick-off is created by combining three adjacent electrodes into a single electrode that subtends approximately 45 degrees. The centroids of the two pick-offs themselves subtend 45 degrees as shown in Fig. 1. The pick-offs are denoted as the S_1 and S_2 electrodes. The electrodes that are antipodal to the pick-offs are used as electrostatic forcers, shown in Fig. 1 as the D_1 and D_2 electrodes. The resonator is biased up to 40 volts and the forcer electrode potentials are specified about a mean of 0 volts. The pick-off electrodes are buffered by high-gain trans-resistance amplifiers that hold the pick-off electrode at ground potential. The current induced on the electrode by a change in the resonator-electrode gap is amplified into a low impedance voltage. All unused electrodes are held at either ground potential or at the gyro bias for the duration of the deposition experiments.

Resonators are tested at a pressure lower than 1 mT. In a typical experiment the forcer electrodes are directly driven by test signals generated from a digital signal processor. The subsequent response of the resonator is measured as the trans-resistance amplifier output voltage. Multi-channel test data are recorded and analyzed to generate frequency responses using standard auto- and cross-spectral estimation. The test signals are usually chosen to be band-limited chirps with energy concentrated around the modes of interest. Fig. 6 shows a broadband frequency response of a single channel.

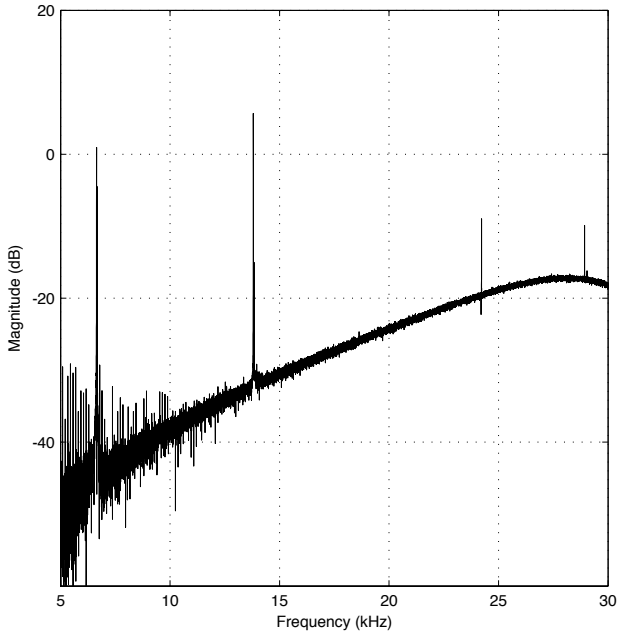

Fig. 6. Broadband frequency response showing the in-plane $n = 1$, $n = 2$, $n = 3$ and $n = 4$ modes near 6.5 kHz, 13.5 kHz, 24.5 kHz, and 29 kHz, respectively. The floor is due to stray capacitance.

III. Resonator Modeling and Mass Deposition Algorithm

The effect of point mass perturbations on the modal frequencies and anti-nodes of a thin ring are first reviewed and a relationship between the frequency detuning (difference in modal frequencies) and anti-node orientations before and after the mass perturbation is derived. This expression is used in a search procedure for enumerating the mass deposition locations that reduce the detuning below a specified threshold. This process is iteratively applied until the frequency detuning is smaller than the resonance bandwidth. Since it is necessary to measure the frequency detuning and anti-node orientations, this section also presents a systematic approach for extracting these parameters from a model that is fit to multi-channel frequency response data. Since the model is developed from the perspective of the built-in electrodes, the electrode arrangement around the resonator establishes a physical reference for the anti-node orientations as well as the angular position of the mass deposition locations.

A. Mass Perturbation Model for a Ring

The relationship between the modal frequencies $\{\omega_1, \omega_2\}$ and anti-node orientations $\{\psi_1, \psi_2\}$ of the in-plane modes with $n = 2$ modal diameters in a perturbed ring resonator are reproduced below from [5],

$$\begin{aligned}
\tan 4\psi_1 &= \frac{\sum_k m_k \sin 4\phi_k}{\sum_k m_k \cos 4\phi_k} \\
\omega_1^2 &= \omega_0^2 \left(\frac{(1+\alpha_2^2) M_0}{M(1+\alpha_2^2) - (1-\alpha_2^2) \sum_k m_k \cos 4(\phi_k - \psi_1)} \right) \\
\omega_2^2 &= \omega_0^2 \left(\frac{(1+\alpha_2^2) M_0}{M(1+\alpha_2^2) + (1-\alpha_2^2) \sum_k m_k \cos 4(\phi_k - \psi_1)} \right)
\end{aligned} \tag{1}$$

where m_k, $k = 1, \ldots, N_m$, represent the perturbing point masses, and ϕ_k the corresponding angular location on the ring relative to a ring-fixed coordinate system, M_0 is the nominal ring mass and $M = M_0 + \sum_k m_k$ is the perturbed ring mass. Furthermore, ω_0 represents the natural frequency of the degenerate modes of the unperturbed perfect ring and α_2 the amplitude ratio of the radial and tangential displacement for modes with $n = 2$ modal diameters. The notation in [5] is largely retained, and although the $n = 2$ case is studied exclusively in this paper, the results developed below can be extended to any pair of nominally degenerate modes. The anti-node orientation associated with the ω_1 mode is is given by ψ_1 and the analysis in [5] assumes $\psi_2 = \psi_1 + 45°$.

The present paper uses (1) as a starting point but manipulates these equations into a form that is more conducive to inserting parameters that can be readily determined from experiments. The analysis will be developed for a ring and then extended to the resonator of Sec. II. The following is derived from (1),

$$\begin{aligned}
\frac{\omega_0^2}{\omega_2^2} - \frac{\omega_0^2}{\omega_1^2} &= \frac{2(1-\alpha_2^2)}{M_0(1+\alpha_2^2)} \sum_{k=1}^{N_m} m_k \cos 4(\phi_k - \psi_1) \\
&= \frac{2(1-\alpha_2^2)}{M_0(1+\alpha_2^2)} \left[\left(\sum_{k=1}^{N_m} m_k \cos 4\phi_k \right) \cos 4\psi_1 \right. \\
&\quad \left. + \left(\sum_{k=1}^{N_m} m_k \sin 4\phi_k \right) \sin 4\psi_1 \right].
\end{aligned} \tag{2}$$

The left-hand side can be rewritten as $\omega_0^2(\omega_1 - \omega_2)(\omega_1 + \omega_2)/(\omega_2^2\omega_1^2)$ and at this point a reasonable approximation is made: $\omega_1/\omega_0 \approx \omega_2/\omega_0 \approx 1$ so that $\omega_0^2(\omega_1 + \omega_2)/(\omega_2^2\omega_1^2) \approx \frac{2}{\omega_0}$. This approximation is justified since the original frequencies and the final tuned frequencies are within 0.2% for the resonators considered in this paper. Furthermore, when (2) is adapted for purposes of developing an iterative tuning algorithm, there are other error sources associated with experimentally measured quantities that dominate the uncertainty of the predicted frequency split. Thus, for resonators in which difference in perturbed frequencies is orders of magnitude smaller than their nominal values, we may assume equality with the understanding that this relation predicts the frequency difference to within a few tenths of a percent,

$$\begin{aligned}
\omega_1 - \omega_2 = \omega_0 \frac{1-\alpha_2^2}{M_0(1+\alpha_2^2)} &\left[\left(\sum_{k=1}^{N_m} m_k \cos 4\phi_k \right) \cos 4\psi_1 \right. \\
&\left. + \left(\sum_{k=1}^{N_m} m_k \sin 4\phi_k \right) \sin 4\psi_1 \right].
\end{aligned} \tag{3}$$

The solder sphere or ink deposition described in Sec. II provides a quantized amount of mass, though, so (3) is modified such that each mass m_k is replaced by the fixed mass quanta denoted m_0,

$$\omega_1 - \omega_2 = \gamma \left(\sum_{k=1}^{N_m} \cos 4\phi_k \right) \cos 4\psi_1 + \gamma \left(\sum_{k=1}^{N_m} \sin 4\phi_k \right) \sin 4\psi_1, \tag{4}$$

where $\gamma = \omega_0 m_0(1-\alpha_2^2)/(M_0(1+\alpha_2^2))$ is a *sensitivity parameter* that is associated with the quantized mass m_0. Sec. IV-A describes how γ is experimentally estimated. Given an initially perfect ring resonator with nominal $n=2$ modal frequencies equal to ω_0, (4) and the $\tan 4\psi_1$ relation in (1) can be used to predict the difference in modal frequencies and the anti-node orientations after perturbing the ring with N_m masses of mass m_0 at locations $\{\phi_k\}$, $k=1,\ldots,N_m$.

The inverse trimming problem in which an imperfect ring is to be mass loaded so that the modal frequency difference is eliminated is also governed by (4). In this case, the initial *imbalance parameters* associated with the $n=2$ pair of modes, denoted σ_c and σ_s, are defined to be

$$\begin{aligned}\sigma_c &= \omega_0 \frac{1-\alpha_2^2}{M_0(1+\alpha_2^2)} \sum_{k=1}^{N_m} m_k \cos 4\phi_k \\ \sigma_s &= \omega_0 \frac{1-\alpha_2^2}{M_0(1+\alpha_2^2)} \sum_{k=1}^{N_m} m_k \sin 4\phi_k\end{aligned} \tag{5}$$

so that (3) can be written

$$\omega_1 - \omega_2 = \sigma_c \cos 4\psi_1 + \sigma_s \sin 4\psi_1. \tag{6}$$

Also note $\tan 4\psi_1 = \sigma_s/\sigma_c$. The imbalance parameters can be estimated from measurements of the mismatched frequencies and antinode orientation, in other words,

$$\begin{aligned}\sigma_c &= (\omega_1 - \omega_2)\cos 4\psi_1 \\ \sigma_s &= (\omega_1 - \omega_2)\sin 4\psi_1.\end{aligned} \tag{7}$$

Although (5) appears to imply the that imbalance parameters are a consequence of mass perturbations, this need not be the case, and in practice the imbalance parameters are defined using (7) after the modal frequencies and anti-node orientations are measured. Subsequent mass perturbation of the resonator will modify the frequency mismatch according to

$$\begin{aligned}\tilde{\omega}_1 - \tilde{\omega}_2 = &\left(\sigma_c + \gamma \sum_{k=1}^{N_m} \cos 4\phi_k\right) \cos 4\tilde{\psi}_1 \\ &\left(\sigma_s + \gamma \sum_{k=1}^{N_m} \sin 4\phi_k\right) \sin 4\tilde{\psi}_1\end{aligned} \tag{8}$$

where $\tilde{\omega}_1 - \tilde{\omega}_2$ represents the post-perturbation difference in modal frequency and where the new anti-node orientation $\tilde{\psi}_1$ satisfies

$$\tan 4\tilde{\psi}_1 = \frac{\sigma_s + \gamma \sum_{k=1}^{N_m} \sin 4\phi_k}{\sigma_c + \gamma \sum_{k=1}^{N_m} \cos 4\phi_k}. \tag{9}$$

A compact expression relating the pre- and post-perturbation frequency differences and anti-node orientations can be derived from (8) and (9),

$$\tilde{\Delta} e^{j4\tilde{\psi}_1} = \Delta e^{j4\psi_1} + \gamma \sum_{k=1}^{N_m} e^{j4\phi_k} \tag{10}$$

where $\Delta = \omega_1 - \omega_2$ and ψ_1 are the pre-perturbation frequency difference and anti-node orientation, respectively, and $\tilde{\Delta} = \tilde{\omega}_1 - \tilde{\omega}_2$ and $\tilde{\psi}_1$ are the post-perturbation frequency difference and anti-node orientation, respectively, and $j=\sqrt{-1}$.

The objective is to eliminate the imbalance parameters by judicious choice of the quantity of added mass and their corresponding locations, in other words, it is desired to select ϕ_k such that

$$\begin{aligned}\sigma_c + \gamma \sum_{k=1}^{N_m} \cos 4\phi_k = 0 \\ \sigma_s + \gamma \sum_{k=1}^{N_m} \sin 4\phi_k = 0\end{aligned} \tag{11}$$

It is generally not possible to achieve (11), though, because of the quantized mass and quantized deposition locations, however, the fine and coarse mass perturbations introduced in Sec. II-B do allow reduction of the modal frequency mismatch to such a degree that the benefits of degenerate modal frequencies are fully realized.

B. Extending the Ring Mass Perturbation Model

The frequency difference and anti-node orientation relation (10) can be extended from a simple ring to the resonator in Sec. II. The issue is that the sensitivity parameters associated with the $n=2$ modes depend on which layer (radius) of the nested spokes the mass deposition is performed. The outboard spokes accept the ink droplet perturbations and the sensitivity associated with a single droplet on an outboard spoke is denoted γ_1. Similarly, the next inboard layer of spokes that accept the solder sphere deposition possess sensitivity γ_2 with regard to a single solder sphere. The remaining two layers of spokes that accept solder sphere deposition possess sensitivities γ_3 and γ_4, with γ_4 being associated with the most inboard layer of large spokes. Thus, (10) is modified to

$$\begin{aligned}\tilde{\Delta} e^{j4\tilde{\psi}_1} = &\Delta e^{j4\psi_1} + \gamma_1 \sum_{k=1}^{N_1} e^{j4\phi_k^{(1)}} + \gamma_2 \sum_{k=1}^{N_2} e^{j4\phi_k^{(2)}} \\ &+ \gamma_3 \sum_{k=1}^{N_3} e^{j4\phi_k^{(3)}} + \gamma_4 \sum_{k=1}^{N_4} e^{j4\phi_k^{(4)}}.\end{aligned} \tag{12}$$

where N_1 is number of ink droplets deposited at positions $\phi_k^{(1)}$, N_2 is the number of solder spheres deposited with sensitivity γ_2 at positions $\phi_k^{(2)}$ and so forth. Although *ad hoc*, this extension performs very well in practice and relies on the deflection of the various layers of spokes for a given mode to conform to the mode shape associated with the ring, albeit with different relative amplitudes, and, hence, different sensitivity parameter values, but with the same anti-node orientation.

C. Estimating ψ and Δ from Frequency Domain Models

Estimates of ω_1, ω_2, and ψ_1 are required to guide the mass deposition process. A model-based approach for extracting this information from empirical frequency response data is now described and offers an efficient alternative to estimating the nodes/anti-node with a vibrometer, for example. The $n=2$ anti-nodes subtend an approximately 45° angle between them so the forcer and pick-off electrode configuration shown in Fig. 1 are arranged to optimally excite and sense the $n=2$ pair. This forcer and pick-off configuration guarantees that a

two-mode model can be fit to the data even when the modal frequencies are degenerate, that is $\Delta = 0$.

The two forcer electrodes and two pick-off electrodes are used to generate a two-input/two-output empirical frequency response of the resonator dynamics in a narrow frequency band encompassing the $n = 2$ modes. Although a single channel of measurement data can be adequate for estimating the modal frequencies when their difference is sufficiently large, it is not possible to uniquely determine the anti-node orientations, thus, additional independent forcers and pick-offs are necessary to resolve the anti-nodes. Furthermore, when the frequency mismatch is relatively small, a single channel of measurement data is not enough to discriminate both modes, especially if one mode dominates the measurement channel. Once the two-input/two-output frequency response data is acquired, the following transfer function model is fit to this data

$$\hat{\mathbf{y}} = (Ms^2 + Cs + K)^{-1} H(s) \hat{\mathbf{u}} \tag{13}$$

where $\hat{\mathbf{y}}$ and $\hat{\nu}$ are Laplace transforms of the two-channel pick-off signals and two-channel forcer voltage signals, respectively, M, C, and K are positive definite mass, damping and stiffness matrices, respectively, and s is the Laplace transform variable. It is also necessary to introduce a low-order polynomial transfer function, denoted H, to capture the effects of buffer and signal conditioning dynamics and any other out-of-band resonator dynamics that may contribute phase and magnitude offsets in the frequency response data in a neighborhood of the $n = 2$ modes. The $n = 2$ modes are well-isolated from other modes in the resonator so M, C, and K can be taken to be 2×2 matrices and this leads to a very convenient formulation of an optimization problem to determine the second order model matrices $\{M, C, K\}$. The reader is referred to [17] where the parameter fitting is discussed in detail and to [18] where it is applied to the modal analysis of another axisymmetric resonator.

The n=2 mode shapes of the outermost ring of resonator in Sec. II are closely approximated by those of a simple ring, which are

$$\begin{aligned} w_k(\theta, t) =& u_0 \alpha_2 \cos\left(2\left(\theta - \psi_k\right)\right) \sin(\omega_k t) \\ u_k(\theta, t) =& u_0 \sin\left(2\left(\theta - \psi_k\right)\right) \sin(\omega_k t) \end{aligned}, \quad k = 1, 2 \tag{14}$$

where w_k and u_k are the radial and tangential displacements with respect to the at-rest circular shape at a location θ on the ring [5]. The amplitude of the tangential motion is denoted u_0 and $\alpha_2 \approx 2$ for high aspect ratio rings. It is assumed that the pick-off electrodes sense only the radial component of the outer ring displacement and since each electrode also subtends a 45° arc, it can be shown that for the $n = 2$ modes, the small radial displacement averaged over the electrode arc is $2\sqrt{2}/\pi$ times the radial displacement at the centroid of the electrode and that this scaling is independent of ψ_i. Thus, the centroids of the pick-off electrodes define a physical coordinate system for the resonator and establish the coordinates in which the $\{M, C, K\}$ parameters in (13) are defined.

The objective is to determine ψ_k from the identified model parameters. The modal frequencies satisfy

$$\left(-\omega_k^2 M + K\right) \mathbf{v}_k = 1, \quad k = 1, 2.$$

where $\{\mathbf{v}_1, \mathbf{v}_2\}$ are the corresponding normalized eigenvectors and the anti-node orientations, ψ_i, can be determined from these eigenvectors. Consider the case in which the resonator is undamped and unforced. If the initial state has zero velocity and is a scalar multiple of one of the two generalized eigenvectors of M and K, then the free response will be a scalar multiple of that eigenvector, i.e.

$$\mathbf{y}(t) = y_0 \cos(\omega_k t) \mathbf{v}_k \quad k \in 1, 2 \tag{15}$$

where y_0 is the scalar displacement magnitude of the initial state. On the other hand, the time response $\mathbf{y}(t)$ can also be found by using the approximate mode shape,

$$\begin{aligned} \mathbf{y}(t) &= \frac{2\sqrt{2}}{\pi} k_e \begin{bmatrix} w_k(\theta_1, t) \\ w_k(\theta_2, t) \end{bmatrix} \\ &= \frac{2\sqrt{2}}{\pi} k_e \alpha_2 u_0 \begin{bmatrix} \cos(2(\theta_1 - \psi_k)) \\ \cos(2(\theta_2 - \psi_k)) \end{bmatrix} \cos(\omega_k t) \\ &= \frac{2\sqrt{2}}{\pi} k_e \alpha_2 u_0 \begin{bmatrix} \cos(2\theta_1) & \sin(2\theta_1) \\ \cos(2\theta_2) & \sin(2\theta_2) \end{bmatrix} \begin{bmatrix} \cos(2\psi_k) \\ \sin(2\psi_k) \end{bmatrix} \cos(\omega_k t). \end{aligned} \tag{16}$$

where k_e represents the pick-off electrode displacement-to-voltage gain, and θ_1 and θ_2 represent the centroids of the S_1 and S_2 pick-off electrodes with respect to a resonator-fixed coordinate system. As previously described, the angle reference passes through the centroid of the S_1 electrode (see Fig. 1) so $\theta_1 = 0^\circ$ and $\theta_2 = 45^\circ$ radians. Equating (15) and (16) yields,

$$\psi_k = \frac{1}{2} \tan^{-1}\left(\frac{\mathbf{e}_2 \cdot \mathbf{v}_k}{\mathbf{e}_1 \cdot \mathbf{v}_k}\right) \tag{17}$$

where the standard unit vectors are defined $\mathbf{e}_1 = \begin{bmatrix} 1 & 0 \end{bmatrix}^T$ and $\mathbf{e}_2 = \begin{bmatrix} 0 & 1 \end{bmatrix}^T$, and $\cdot$ is the scalar product. Thus, estimates for the anti-node orientations in addition to the modal frequencies can be obtained from the identified frequency domain model parameters.

A detailed example demonstrating the systematic reduction of an initial frequency mismatch of 25.41 Hz to 0.06 Hz is given in Sec. IV. The frequency response of the unperturbed resonator that is featured in this example is shown in Fig. 7. Overlaid on the data is the frequency response of the identified model (13) and analysis of this model reveals $\omega_1 = 13530.08\,\text{Hz}$, $\omega_2 = 13504.67\,\text{Hz}$, $\psi_1 = 33.5^\circ$.

IV. Demonstration of Modal Frequency Mistmatch Reduction

A. Estimating the Mass Perturbation Sensitivities

The sensitivity of the modal properties to ink or solder sphere deposition are experimentally determined. Three resonators were chosen on which twelve individual solder sphere depositions (four per resonator) were performed in order to estimate γ_2, γ_3 and γ_4. It is necessary to establish a labeling convention for the model frequencies since the sensitivity parameters are determined with respect to this convention. As suggested by the test data in Sec. III-C, the higher frequency mode is labeled ω_1 with corresponding anti-node orientation ψ_1. Thus, the detuned frequency parameters are defined such that $\Delta = \omega_1 - \omega_2 > 0$. With this convention, all mass

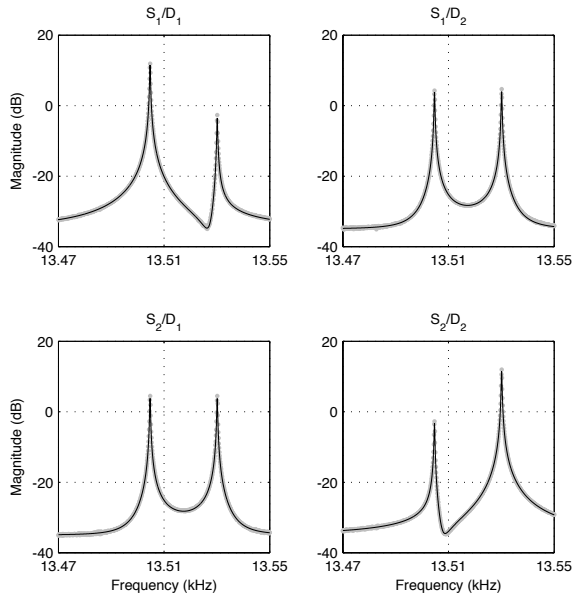

Fig. 7. Empirical frequency response magnitude of the resonator derived from narrow band chirp tests (light grey points) versus the model frequency response (thin black line). This resonator is taken through a series of mass deposition steps described in Sec. IV in order to reduce the initial frequency detuning value $\Delta = 25.41$ Hz.

loading perturbations will have an associated sensitivity that is negative, i.e. $\gamma_k < 0$. For example, in order to determine γ_2, a single solder sphere is deposited on one of the spokes that comprises the most outboard spoke layer that accepts solder spheres. The pre- and post-deposition parameters, $\{\Delta, \psi_1\}$ and $\{\tilde{\Delta}, \tilde{\psi}_1\}$, respectively, are measured and (12) is solved for γ_2,

$$\tilde{\Delta} e^{j4\tilde{\psi}_1} = \Delta e^{j4\psi_1} + \gamma_2 e^{j4\phi_1^{(2)}} \tag{18}$$

where $\phi_1^{(2)}$ is the location of the spoke where the deposition is performed. In the exceptional case where $\phi_1^{(2)} = \psi_1$, then $\tilde{\psi}_1 = \psi_1$ and sensitivity reduces to $\gamma_2 = \tilde{\Delta} - \Delta$. In practice, however, ψ_1 will not bisect a spoke, so a real value of γ_2 is determined according to a least square error criterion. Tests with a single solder sphere were carried out on four separate occasions to estimate γ_2. Analogous tests on different spoke layers were performed for identifying the remaining solder sphere sensitivities γ_3 and γ_4 as well as well as the sensitivity of a single ink droplet. The droplet sensitivity γ_1 was estimated to be approximately 0.05 Hz/droplet but there was a large spread due to the fact that as the ink deposition system was operated, the silver particles would settle and produce droplets with more mass. The solder sphere estimated sensitivities exhibited much greater consistency and the results of these tests are summarized in Table I and show that the sensitivity is inversely proportional to the spoke's radial location. Although this result appears counterintuitive, finite element analysis reveals that for the four layers of spokes where mass deposition can take place, the spoke velocity is actually larger the more inboard the spoke position. This is due to the fact that the higher density of spokes in the outer rings stiffens the structure so that among the four spoke layers where mass is deposited, the most outboard spokes actually have the smallest velocity.

TABLE I
SUMMARY OF SOLDER SPHERE SENSITIVITY EXPERIMENTS

Sensitivity parameter	Mean (Hz)	Standard deviation (Hz)
γ_2	-2.77	0.13
γ_3	-3.30	0.12
γ_4	-3.74	0.16

B. Mass Deposition Procedure Applied to a Resonator

The resonator with the as-fabricated frequency response shown in Fig. 7 is taken through a series of mass deposition steps to reduce Δ from its initial value of 25.41 Hz. The quantized angular locations of the mass perturbations coupled with the 4ϕ dependency, means that there are only 24 unique perturbation positions as far as the $n = 2$ modes are concerned. Of these positions, 18 are associated with the solder spheres and the remaining 6 are associated with ink deposition. The general strategy is to perform two rounds of solder sphere deposition to reduce Δ to approximately 1 Hz so that subsequent ink deposition can be used to reduce Δ below 100 mHz. For the present resonator, it was desired to reduce Δ by about 12 Hz after the first deposition step. This can be achieved with four solder spheres based on the identified sensitivities, so (12) is used as follows: all possible combinations of four solder spheres are evaluated for the nine closest spokes to the identified ψ_1 axis as shown in Fig. 8. In other words, the higher frequency mode is preferentially mass-loaded and will be effected to a greater degree than the lower frequency mode. The computational burden to enumerate these choices is minimal because it requires evaluating (12) 9^4 times and additional criteria can be used to further down-select from the deposition scenarios that yield a reduction of at least 12 Hz (for example, the desire to distribute the mass as symmetrically as possible). The final selection is 3 depositions on the inner-most spokes (corresponding to sensitivity γ_4) at the following positions $\phi_1^{(4)} = 22.5°$, $\phi_2^{(4)} = 37.5°$, and $\phi_3^{(4)} = 37.5°$, and one solder sphere with sensitivity γ_2 at position $\phi_1^{(2)} = 37.5°$. Note that due to the 4ϕ dependency, the solder spheres are arranged in a compass-points pattern to minimize the imbalance of forces exerted on the resonator stem due to the deposition. The 4ϕ dependency also permits the specification of up to four solder sphere at the same angular location because they can be physically arranged as $\phi + n90°$, $n = 0, 1, 2, 3$. This feature is exploited in the first deposition because $\phi_2^{(4)} = \phi_3^{(4)}$. The *predicted* detuning frequency $\tilde{\Delta}$ after the deposition is 12.86 Hz and the measured value is 13.08 Hz. The solder sphere positions and pre- and post-deposition frequency responses are shown in Fig. 8 where $\psi_1 = 33.5°$ and $\tilde{\psi}_1 = 32.0°$.

The second step of mass deposition also employs four solder spheres and the objective is to reduce the frequency detuning to less than 1 Hz. The second step does not exploit the fact that the resonator has already been modified; the modal frequencies and anti-nodes are simply measured and another deposition scenario is selected. Thus, $\psi_1 = 32.0°$ and the next four solder sphere depositions sites are selected to be $\phi_1^{(4)} = 37.5°$, $\phi_1^{(3)} = \phi_2^{(3)} = \phi_3^{(3)} = 30°$. Fig. 9 shows the cumulative

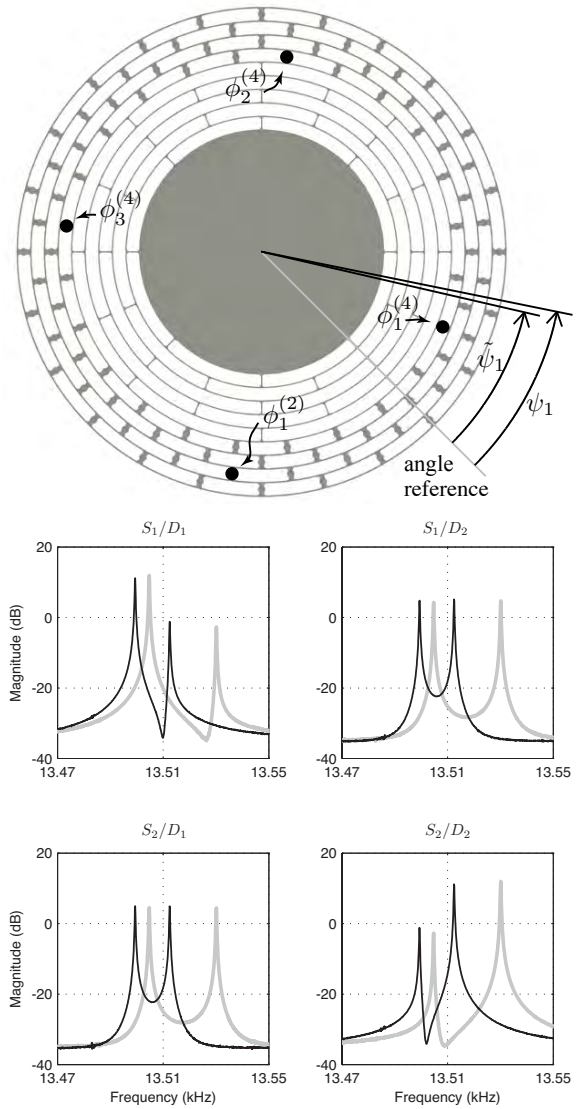

Fig. 8. Top: The ψ_1 anti-node associated with the higher frequency mode is shown for the as-fabricated resonator. Four solder spheres are deposited at the spoke locations shown as black dots. Bottom: The as-fabricated resonator frequency response (light grey trace) compared the frequency response after the first round of deposition (black trace). Only the frequency response data are shown (no model frequency responses are shown). The frequency detuning has been reduced from $\Delta = 25.41$ Hz to $\tilde{\Delta} = 13.08$ Hz.

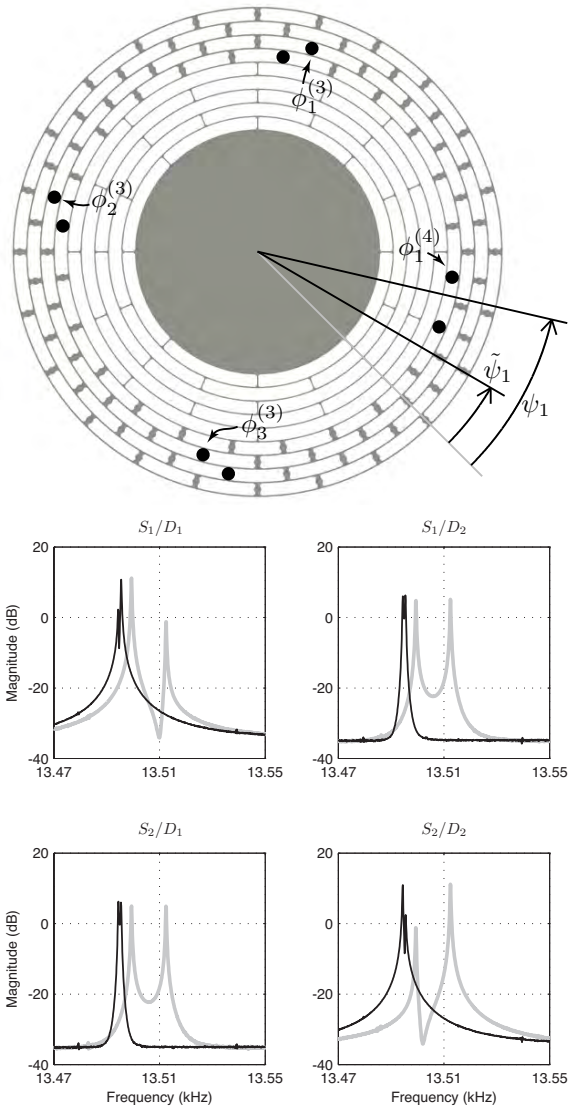

Fig. 9. Top: The ψ_1 anti-node associated with the higher frequency mode is shown before the second round of mass deposition. Four more solder spheres are deposited and complement the spheres deposited in the previous step (the cumulative number of spheres are shown). At the conclusion of the deposition the anti-node orientation is now $\tilde{\psi}_1 = 14.7°$. Bottom: The resonator frequency response after the first round of deposition (light grey trace) is compared the frequency response after the second round of deposition (black trace). The frequency detuning has been reduced from $\Delta = 13.08$ Hz to $\tilde{\Delta} = 1.06$ Hz.

depositions and compares the empirical frequency responses measured at the conclusion of the first deposition to those measured after the second deposition. The *predicted* frequency detuning after this second round of mass deposition is 0.19Hz compared to the measurement of 1.06 Hz. After the second round of deposition, the anti-node orientation is estimated to be $\tilde{\psi}_1 = 14.7°$.

The final deposition round uses the silver particle loaded ink. Since $\psi_1 \approx 15°$, the ink deposition can be made into the reservoirs that effectively lie on the anti-node, in other words, $\phi_k^{(1)} = 15°$, and 25 ink droplets are distributed among the four reservoirs shown in Fig. 10. Due to the uncertainty associated with the droplet mass, an intermediate measurement of the resonator dynamics was performed midway through the ink deposition. Fig. 10 compares the frequency response after the conclusion of the second round of solder sphere deposition to the frequency response after the conclusion of the ink deposition. The final estimated frequency detuning is 60 mHz, which is well within the resonance bandwidth, and the anti-node orientation is $\tilde{\psi}_1 = 70.2°$.

V. Discussion

Four additional resonator examples are summarized in Table II and show the initial frequency detuning and the final detuning achieved after three iterations of mass deposition. These experiments reveal that many different combinations of mass perturbations can adequately reduce the frequency detuning of a resonator. Three different costs are apparent

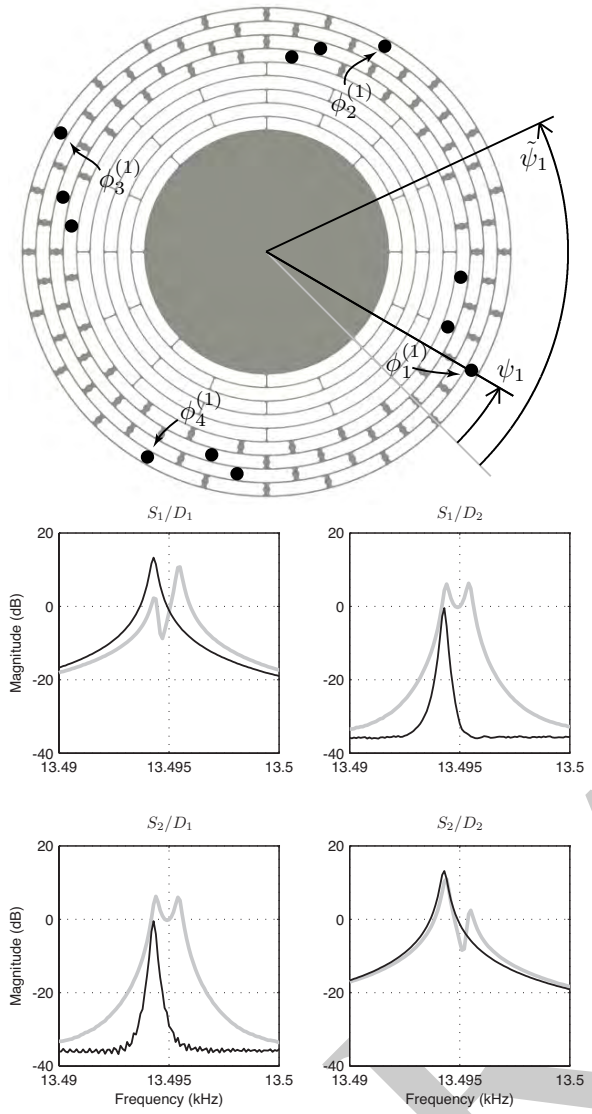

Fig. 10. Top: Ink deposition in the reservoirs along the ψ_1 anti-node is the last step. Bottom: The resonator frequency response after the second round of deposition (light grey trace) is compared the frequency response after the ink deposition (black trace). The frequency detuning has been reduced from $\Delta = 1.06\,\text{Hz}$ to $\tilde{\Delta} = 0.06\,\text{Hz}$.

when modifying a resonator: the total amount of mass that needs to be added to the resonator to achieve a tolerable level of detuning, the total number of iterations required, and the computational cost in evaluating (12) to enumerate the various perturbation choices in each step. An exhaustive search using (12) is not prohibitive so an optimal solution can be determined for any given fixed number of deposited solder spheres. The main decision is the desired reduction in detuning frequency for a given round of deposition. For example, Resonators 4 and 5 have initial frequency detunings exceeding 27 Hz, and an aggressive deposition strategy was employed for these resonators whereby the initial split was to be reduced by at least 25 Hz after the first round of solder sphere deposition. The detuning reduction was successful for these resonators, however, as the number of deposited solder spheres increases in a given step, the deviation from the

TABLE II
DATA SUMMARY FOR FIVE RESONATORS

Resonator #		As fab	Dep #1	Dep #2	Dep #3
1	**s/i**	-	4s	4s	25i
	Δ (Hz)	25.41	13.08	1.06	0.06
	Q (k)	51/51	51/51	51/51	52/52
2	**s/i**	-	4s	2s	3i
	Δ (Hz)	14.17	1.62	0.13	0.08
	Q (k)	52/52	53/53	43/53	53/52
3	**s/i**	-	5s	2s	7i
	Δ (Hz)	16.92	1.28	0.42	0.03
	Q (k)	49/47	51/51	51/51	51/51
4	**s/i**	-	9s	2s	8i
	Δ (Hz)	32.17	5.44	0.35	0.05
	Q (k)	45/47	51/51	40/50	51/51
5	**s/i**	-	9s	1s	8i
	Δ (Hz)	28.50	2.50	0.45	0.03
	Q (k)	55/55	56/56	55/55	55/55

The "s" and "i" denote "solder spheres" and "ink droplets", respectively. Resonator #1 is discussed in detail in Sec IV. Quality factors are denoted by Q.

predicted post-deposition value of detuning also increases due to variations in sphere mass, errors in estimating Δ and ψ_1, and errors in estimating the sensitivity parameters. The most reliable predictions resulted from reducing the large initial detuning over the course of two depositions of more moderate size as described for Resonator 1.

The solder sphere deposition was also performed to minimize the reaction forces and torques on the resonator stem as a result of the added mass, and for the $n = 2$ modes, complete cancellation of the forces and torques would be achieved if for every sphere deposited, three additional spheres at the same radii but $n90^\circ$ from the deposition location, $n = 1, 2, 3$, are also deposited. This can only be approximately achieved in practice as shown in Figs. 8 thru 10. Nevertheless, no degradation in the modal quality factors was noted when comparing the initial Q values to the values after the final deposition and a cleaning step (the quality factors are listed in Table II).

The resolution of the detuning reduction with solder sphere deposition is actually significantly better than what is suggested in Table I. For example, if two solder spheres are deposited at the same radius but their angular locations differ by 45°, then the frequency split remains unchanged because $\gamma(e^{j4\phi} + e^{j4(\phi+\pi/4)}) = 0$, so despite the fact that both modal frequencies *decrease* due to the additional mass, the detuning does not change. Now consider moving one sphere to a different radius, for example let one sphere be located at $\phi_1^{(2)}$ and the other at $\phi_1^{(3)} = \phi_1^{(2)} + 45^\circ$, then $\gamma_2 e^{j4\phi_1^{(2)}} + \gamma_3 e^{j4\phi_1^{(3)}} = (\gamma_2 - \gamma_3)e^{j4\phi_1^{(2)}}$. Thus, the maximum change in frequency detuning cannot exceed the *difference* between the sensitivities, which for the solder spheres is considerably smaller than any given value of γ_2, γ_3 or γ_4. This property is exploited in reducing the detuning below the sensitivities associated with the solder spheres and is the reason why after two iterations of solder sphere deposition,

the frequency detuning is significantly less than the smallest sensitivity listed in Table I.

Finally, from the perspective of testing a resonator, there is practical advantage to working with the detuning frequency Δ instead of absolute modal frequencies. The Sec. II resonators' modal frequencies have an approximate -0.5 Hz/°C dependency so if absolute frequency measurements are used in making mass deposition decisions, the resonator temperature must be regulated to the same value for each test. This is certainly achievable but it adds to the complexity of testing the resonator. On the other hand, because the temperature dependency of each mode is effectively the same for broad temperature range about room temperature, Δ is insensitive to the precise resonator temperature and this facilitates more rapid characterization of its modal properties.

VI. Conclusion

A model-based approach has been developed and applied to a novel micro-resonator to eliminate the as-fabricated difference in modal frequencies of two nominally degenerate modes. The resonator was specifically designed to accommodate point mass perturbations in the form of precision solder spheres and silver particle loaded ink. Although the deposition locations and the mass perturbations themselves are quantized, results were reported for five resonators and showed that the $n = 2$ modal frequency detuning was systematically reduced to less than $80\,\text{mHz}$ in all cases, even when starting from an initial detuning of over $30\,\text{Hz}$. Parametric resonator models were fit to frequency response data and the models were used to determine modal frequencies and anti-node orientations. This approach is in contrast to more traditional vibrometer-based techniques in which the anti-nodes are located by scanning the vibrometer spot across the resonator as a single mode is excited. The testing time is significantly reduced with the modeling approach because the frequency response data can be gathered in just a few minutes.

There are a number of potential directions for future research. A recent result by the authors reports on the performance of the resonator operated as a force-to-rebalance vibratory gyro and shows how the anti-node orientation with respect to the pick-offs/forcers can impact the noise associated with sensor's the zero rate bias [19]. Thus, it is useful to be able to specify the anti-node orientation as well as the maximum tolerable frequency detuning. The challenge lies in systematically changing ψ, though, because it becomes very sensitive to the perturbations when the frequency detuning becomes small (note the change in ψ in Figs. 9 and 10). Multi-mode tuning is discussed in [5] and an approach is presented to minimize the number of mass perturbations in order to achieve the tuning objectives, however, these results don't obviously extend to the present resonator because of the mass and deposition location quantization constraints. Nevertheless, it may be possible to simultaneously reduce the frequency detuning of the $n = 2$ and $n = 3$ modes, however, such results will be left for future publications.

Acknowledgement

The authors acknowledge the financial support of the Defense Advanced Research Projects Agency and thank the MTO/microPNT program managers Dr. Andrei Shkel and Dr. Robert Lutwak. The authors also thank Tom Lorentz for assistance with the ink deposition system.

References

[1] D.-J. Kim and R. M'Closkey, "Spectral analysis of vibratory gyro noise," *IEEE Sensors J.*, vol. 13, pp. 4361–4374, Nov. 2013.

[2] D. Lynch, "Coriolis vibratory gyros," in *Symp. Gyro Technology*. Stuttgart, Germany: Inst. A für Mechanik, 1998, pp. 1.0–1.14.

[3] D. Allaei, W. Soedel, and T. Y. Yang, "Natural frequencies and modes of rings that depart from perfect axisymmetry," *J. Sound and Vibration*, vol. 111, no. 1, pp. 9–27, 1986.

[4] C. Fox, "A simple theory for the analysis and correction of frequency splitting in slightly imperfect rings," *J. Sound and Vibration*, vol. 142, no. 2, pp. 227–243, 1990.

[5] A. Rourke, S. McWilliam, and C. Fox, "Multi-mode trimming of imperfect rings," *J. Sound and Vibration*, vol. 248, no. 4, pp. 695–724, 2001.

[6] F. Ayazi and K. Najafi, "A HARPSS polysilicon vibrating ring gyroscope," *IEEE J. Microelectromech. Syst.*, vol. 10, pp. 169–179, June 2001.

[7] B. Gallacher, J. Hedley, J. Burdess, A. Harris, A. Rickard, and D. King, "Electrostatic correction of structural imperfections present in a micror-ing gyroscope," *IEEE J. Microelectromech. Syst.*, vol. 14, pp. 221–234, April 2005.

[8] A. Challoner, H. Ge, and J. Liu, "Boeing disc resonator gyroscope," in *Proc. 2014 IEEE/ION Position, Location and Navigation Symp.*, Monterey, CA, May 2014, pp. 504–514.

[9] S. Nitzan, C. Ahn, T.-H. Su, M. Li, E. Ng, S. Wang, Z. Yang, G. O'Brien, B. Boser, T. Kenny, and D. Horsley, "Epitaxially-encapsulated polysilicon disk resonator gyroscope," in *Proc. IEEE MEMS*, Taipei, Jan. 2013, pp. 625–628.

[10] P. Shao, C. Mayberry, X. Gao, V. Tavassoli, and F. Ayazi, "A polysilicon microhemispherical resonating gyroscope," *J. Microelectromech. Syst.*, vol. 23, pp. 762–764, Aug 2014.

[11] P. Taheri-Tehrani, T.-H. Su, A. Heidari, G. Jaramillo, C. Yang, S. Akhbari, H. Najar, S. Nitzan, D. Saito, L. Lin, and D. Horsley, "Micro-scale diamond hemispherical resonator gyroscope," in *Proc. Solid-State Sensors, Actuators and Microsystems Workshop*, Hilton Head, SC, June 2014, pp. 289 – 292.

[12] D. Senkal, M. Ahamed, A. Trusov, and A. Shkel, "Achieving sub-hz frequency symmetry in micro-glassblown wineglass resonators," *IEEE J. Microelectromech. Syst.*, vol. 23, pp. 30–38, Feb 2014.

[13] J. Y. Cho, J.-K. Woo, J. Yan, R. Peterson, and K. Najafi, "Fused-silica micro birdbath resonator gyroscope (μ-BRG)," *IEEE J. Microelectromech. Syst.*, vol. 23, no. 1, pp. 66 – 77, Feb 2014.

[14] J. Cho, J. Gregory, and K. Najafi, "High-Q, 3kHz single-crystal-silicon cylindrical rate-integrating gyro (CING)," in *Proc. IEEE MEMS*, Paris, Jan 2012, pp. 172–175.

[15] B. Gallacher, J. Hedley, J. Burdess, A. Harris, and M. McNie, "Multi-modal tuning of a vibrating ring using laser ablation," *Proc. Inst. Mech. Eng., Part C*, vol. 217, no. 5, pp. 557–576, 2003.

[16] J. Bernstein, M. Bancu, E. Cook, T. Henry, P. Kwok, T. Nyinjee, G. Perlin, W. Teynor, and M. Weinberg, "Diamond hemispherical resonator fabrication by isotropic glass etch," in *Proc. Solid-State Sensors, Actuators and Microsystems Workshop*, Hilton Head, SC, June 2014, pp. 273–276.

[17] D.-J. Kim and R. M'Closkey, "A systematic method for tuning the dynamics of electrostatically actuated vibratory gyros," *IEEE Trans. Control Syst. Technol.*, vol. 14, pp. 69–81, Jan. 2006.

[18] D. Schwartz, D. Kim, and R. M'Closkey, "Frequency tuning of a disk resonator gyro via mass matrix perturbation," *J. Dyn. Syst. Meas. Control*, vol. 131, no. 6, pp. 1–12, 2009.

[19] D.-J. Kim and R. M'Closkey, "A MEM vibratory gyro with mode-mathcing achieved by resonator mass loading," in *Proc. 2014 IEEE/ION Position, Location and Navigation Symp.*, Monterey, CA, May 2014, pp. 499–503.